atoms inside it. Indeed, $La_2@C_{82}$ (4) has been synthesized. Even more interesting in view of our findings is the recent synthesis of $Sc_3@C_{82}$ (7, 8), for which the three Sc atoms have been experimentally identified as occupying three equivalent positions. Because Sc has the same electronic configuration as La and is significantly smaller, it is not surprising that an endohedral three-atom cluster can form. The equivalency of the three positions strongly suggests that the cage does have C_{3v} symmetry and that the Sc atoms have the K configuration.

The behavior we have discovered for $La@C_{82}$ is consistent with the available experimental data. Moreover, the behavior of the other group IIIB metal atoms is similar to that of La; they form similar endohedrally doped fullerenes and, in the case of C_{82}, give three electrons to the cage. Thus we believe that our results are qualitatively valid for those systems also and that they provide insight into them. Contrary to the structure in alkali-intercalated compounds such as K_3C_{60}, endohedral doping of fullerenes with a three-valent atom such as La results not in mere electron donation but in a strong modification of the metal and cage electron states. This modification changes the electronic and vibrational properties of these systems significantly. Particularly interesting would be the properties of solid La-doped fullerenes.

REFERENCES AND NOTES

1. H W. Kroto *et al*, *Nature* **318**, 162 (1985)
2. J. R. Heath *et al.*, *J. Am. Chem. Soc.* **107**, 7779 (1985).
3. T. Pradeep *et al.*, *ibid.* **114**, 2272 (1992).
4. Y. Chai *et al.*, *J. Phys. Chem.* **95**, 7564 (1991).
5. R. D. Johnson *et al*, *Nature* **355**, 239 (1992).
6. J. H. Weaver *et al.*, *Chem. Phys. Lett.* **190**, 460 (1992).
7. C. S. Yannoni *et al.*, *Science* **256**, 1191 (1992).
8. H Shinohara *et al.*, *Nature* **357**, 52 (1992).
9. M. M. Alvarez *et al.*, *J. Phys. Chem.* **95**, 10561 (1991).
10. E. G Gillan *et al*, *ibid.* **96**, 6869 (1992)
11. W Kratschmer *et al.*, *Nature* **347**, 354 (1990).
12. H. W. Kroto, *ibid.* **329**, 529 (1987).
13. D. E. Manolopoulos and P. W. Fowler, *Chem. Phys. Lett.* **187**, 1 (1991); *Nature* **355**, 428 (1992).
14. A. H. H. Chang, W. C. Ermler, R. M. Pitzer, *J. Chem Phys.* **94**, 5004 (1992).
15. R. Car and M. Parrinello, *Phys. Rev Lett.* **55**, 2471 (1985).
16. B. P. Feuston, W. Andreoni, M. Parrinello, E. Clementi, *Phys. Rev. B* **44**, 4056 (1991).
17. G. B. Bachelet, D. R Hamann, M. Schluter, *ibid.* **26**, 4199 (1982).
18. R C. Weast, Ed., *CRC Handbook of Chemistry and Physics* (CRC Press, Boca Raton, FL, ed. 69, 1988–89), p. B-215.
19. L. Kleinman and D. M. Bylander, *Phys. Rev. Lett.* **48**, 1425 (1982).
20. K. Kikuchi *et al.*, *Nature* **357**, 142 (1992).
21. B. L. Zhang, C. Z. Wang, K M. Ho, *Chem. Phys. Lett.* **193**, 225 (1992).

22. We are grateful to R. E Smalley for stimulating us to pursue this research. We also acknowledge useful discussions with P. W. Fowler, R. Johnson, S. Massidda, U. Rothlisberger, R. L. Whetten, C. S. Yannoni, and C. Yeretzian and the help of J. Shelley with the graphics.

20 July 1992, accepted 21 September 1992

Scanning Tunneling Microscopy of Electrodeposited Ceramic Superlattices

Jay A. Switzer,* Ryne P. Raffaelle, Richard J. Phillips, Chen-Jen Hung, Teresa D. Golden

Cleaved cross sections of nanometer-scale ceramic superlattices fabricated from materials of the lead-thallium-oxygen system were imaged in the scanning tunneling microscope (STM). The apparent height differences between the layers were attributed to composition-dependent variations in local electrical properties. For a typical superlattice, the measured modulation wavelength was 10.6 nanometers by STM and 10.8 nanometers by x-ray diffraction. The apparent height profile for potentiostatically deposited superlattices was more square than that for galvanostatically deposited samples. These results suggest that the composition follows the applied potential more closely than it follows the applied current. The x-ray diffraction pattern of a superlattice produced under potential control had satellites out to the fourth order around the (420) Bragg reflection.

Quantum confinement of carriers in nanometer-scale materials leads to size-dependent optical and electrical properties that are intermediate between those of molecules and those of extended network solids (*1*–*3*). As the dimensions of these materials approach the nanometer scale, characterization becomes increasingly more difficult. In multiple quantum wells the composition profile is often designed to be square, yet this profile can only be inferred from x-ray diffraction (*4*–*6*). We have used the STM to measure the modulation wavelength and estimate the squareness of the composition profile in cleaved cross sections of superlattices by mapping out the electronic properties in real space on a nanometer scale. We define a superlattice as a crystalline multilayer structure with coherent stacking of atomic planes and periodic modulation of the structure or composition, or both.

Graduate Center for Materials Research, University of Missouri–Rolla, Rolla, MO 65401.

*To whom correspondence should be addressed.

Operation of the STM is based on the tunneling of electrons due to an applied bias voltage between a conductive sample and a sharp metal tip that are separated by a few nanometers (*7*, *8*). The current density for free electron tunneling through a planar barrier with an applied voltage less than the work function of either the probe tip or the sample is given by

$$J = \left(\frac{e^2}{h}\right)\left(\frac{\kappa}{2\pi s}\right) V \exp(-2\kappa s) \quad (1)$$

where s is the effective tunneling distance, κ is the inverse decay length of the wave function density outside the surface, V is the bias voltage, e is the electronic charge, h is Planck's constant, and $2\kappa = 1.025\phi^{1/2}$. The effective barrier height, ϕ, is, to a first-order approximation, the average of the probe tip and sample work functions (*9*). In the case of nonfree electrons and nonplanar barriers, the tunneling current can no longer be expressed in such simple closed form. The prefactor will be altered as a result of density of states effects (*7*). However, the tunneling current will still have the same exponential dependence on both the sample-to-probe tip separation and the work function.

The work function of a semiconductor is strongly dependent on doping. Using Si as a prototypical material, we find that the calculated work function shifts from 4.6 eV for intrinsic Si to 4.3 eV when the material is doped with only 2×10^{-5} atomic percent (that is, 10^{16} atoms/cm^3) of an *n*-type dopant such as P (*10*). Hence, small changes in doping levels could bring about large contrasts or apparent height differences in the STM.

Another possible source of contrast in semiconducting samples is the local resistance. The surface potential in a nonmetallic sample can be appreciably different from the applied potential resulting from *iR* (current multiplied by resistance) drop in the sample. Again using the example of Si, we find that the resistivity shifts from 2×10^5 ohm-cm for intrinsic Si to 0.4 ohm-cm when the Si is doped with only 2×10^{-5} atomic percent of an *n*-type dopant. Flores and Garcia have estimated that the spreading resistance (resistivity of the semiconductor divided by four times the tip radius) during an STM experiment will be 4×10^8 ohms for a Si sample with a resistivity of 10 ohm-cm (*11*). The relevant V in Eq. 1 is the difference in local surface potentials for the tip and the sample rather than the applied bias.

The sensitivity of the STM to surface

electronic properties has been exploited in the study of charge density waves (*12*), superconductors (*13*), conducting polymers (*14*), semiconductor junctions (*15*), and multiple quantum wells (*16–19*). Osaka *et al.* have shown that the apparent height difference between layers in cleaved GaAs/GaAlAs multiple quantum wells is the result of variations in electronic properties rather than physical corrugation (*16*).

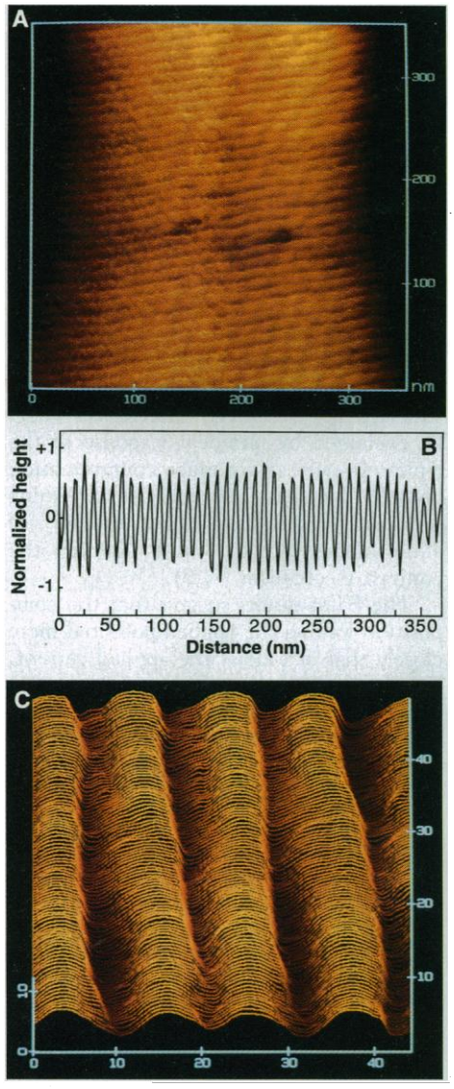

Fig. 1. STM images and cross-sectional profile of a Pb-Tl-O superlattice deposited by pulsing the current density between 0.05 and 5.0 mA/cm^2. The layers are designed to be 5 nm thick, giving a modulation wavelength of 10 nm. (**A**) Top-view image of the cleaved superlattice. The alternating layers are about ten unit cells thick. (**B**) Cross-sectional profile taken from the top-view image. A Fourier transform of this profile gives a modulation wavelength of 10.6 nm, compared with 10.8 nm as measured by x-ray diffraction. (**C**) Higher magnification line plot of the superlattice. The apparent height profile is not square, and it is not possible to identify the beginning and end of each layer.

We report STM studies of cleaved electrodeposited ceramic superlattices based on the Pb-Tl-O system. We have shown that we can deposit superlattices with nanometer-scale layers by galvanostatic pulsing. The modulation wavelengths measured by x-ray diffraction were in good agreement with those calculated for 100% Faradaic efficiency (*20*). One question that remained unanswered in the previous work was whether the composition profile in the superlattice was as square as the applied galvanostatic wave form. The x-ray patterns for the superlattices exhibited first-order satellites with an intensity approximately 5% of the Bragg peak, but higher order satellites were either not observed or had very low intensities. The absence of higher order satellites can indicate that the interfaces are not abrupt and that the composition profile is sinusoidal (*5, 6, 21*). Because superlattices can be deposited by modulating either the potential or the current, it is important to determine which technique provides the best control of composition.

The superlattices in this study are multilayered Pb-Tl oxides in which alternating layers have different compositions. The oxides in this series are interesting because they exhibit the high electrical conductivity of metals with the optical properties of semiconductors. The end members of the series, Tl_2O_3 and PbO_2, are *n*-type degenerate semiconductors with bandgaps of 1.4 and 1.8 eV, respectively (*22–24*). As can be seen in Table 1, either the potential or the current can be systematically varied to control the composition. The potentials in Table 1 are steady-state values that result from the applied current density. All the oxides in this series have a face-centered-cubic Bravais lattice, and the lattice parameters vary by less than 0.3% (*20*). The resistivities of the films deposited under galvanostatic control are also listed in Table 1. The resistivity decreases from 3.0 mohm-cm for a film deposited at 0.05 mA/cm^2 to 1.0 mohm-cm for a film deposited at 5.0 mA/cm^2.

Figure 1 shows STM images and a cross-sectional profile of a superlattice deposited by pulsing the current density between 0.05 and 5.0 mA/cm^2 (*25*). The sample was imaged in air, with no etch treatment to improve contrast (*26*). The dwell times at each current density were chosen to produce a superlattice with equal layer thicknesses and a modulation wavelength (that is, the sum of the alternating layer thicknesses) of 10 nm (*27*). Because the average cubic lattice parameter for the Pb-Tl oxides is 0.536 nm, each layer in the superlattice is approximately ten unit cells thick. The modulation wavelength measured by x-ray diffraction was 10.8 nm. A Fourier transform of the cross-sectional profile from the

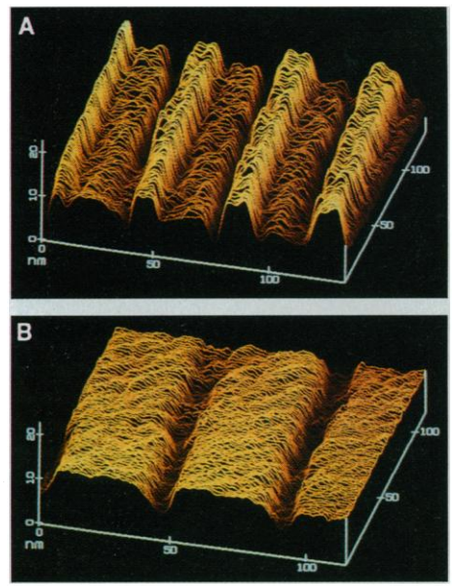

Fig. 2. STM images of cleaved superlattices deposited by pulsing the applied potential between 60 and 270 mV versus SCE. The individual layers are easily identified. In both images the layer with the lower Pb content and higher resistivity has a higher apparent height in the STM image. (**A**) The Tl-rich layer (grown at 60 mV) is 11 nm thick, and the Pb-rich layer (grown at 270 mV) is 34 nm thick. (**B**) The Tl-rich layer is 31 nm thick, and the Pb-rich layer is 16 nm thick.

Table 1. Composition and resistivity of electrodeposited oxide films as a function of applied current density and measured potential versus SCE. The Pb and Tl contents were determined by wavelength-dispersive x-ray analysis in the scanning electron microscope. The oxygen contents were calculated on the assumption that Pb and Tl are in the tetravalent and trivalent oxidation states, respectively.

Applied current density (mA/cm^2)	Measured potential (mV versus SCE)	Film composition	Resistivity (mohm-cm)
0.05	82	$Pb_{0.46}Tl_{0.54}O_{1.7}$	3.0
0.1	93	$Pb_{0.52}Tl_{0.48}O_{1.8}$	2.1
0.5	131	$Pb_{0.59}Tl_{0.41}O_{1.8}$	1.3
1.0	151	$Pb_{0.61}Tl_{0.39}O_{1.8}$	1.2
5.0	250	$Pb_{0.74}Tl_{0.26}O_{1.9}$	1.0

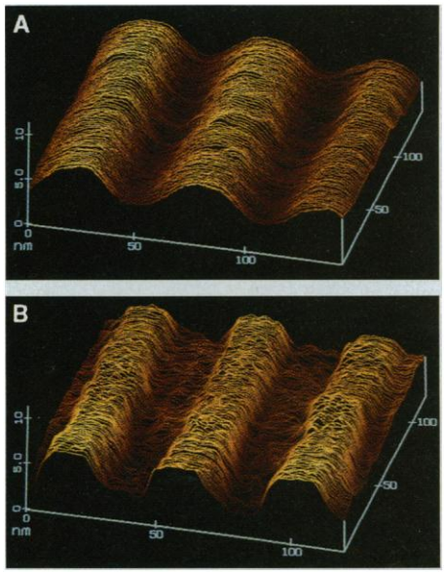

Fig. 3. Comparison of STM lineplot images of superlattices grown under current (**A**) and potential (**B**) control. Both superlattices were designed to have a modulation wavelength of 50 nm. (A) The Tl-rich layer is 30 nm thick, and the Pb-rich layer is 20 nm thick. (B) Both layers are 25 nm thick. The apparent height profile of the potential-controlled superlattice is more square than that of the current-controlled superlattice.

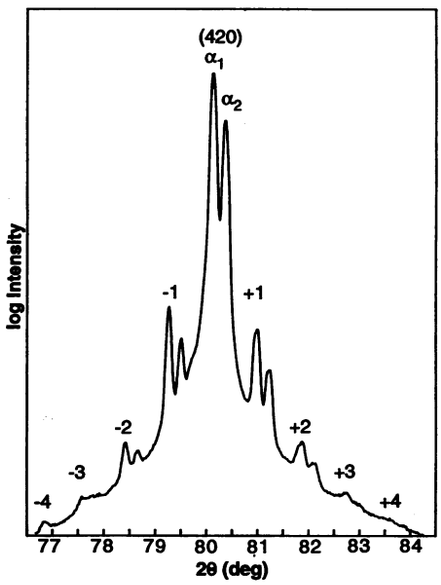

Fig. 4. X-ray diffraction pattern of a superlattice produced under potential control. Superlattice satellites out to the fourth order are seen around the (420) Bragg reflection. The modulation wavelength calculated from the satellites is 13.4 nm. The x-ray radiation is Cu Kα. The splitting of the peaks is caused by the presence of α_1 and α_2 radiation (wavelengths of 0.1540562 and 0.1544390 nm, respectively).

STM image gives a modulation wavelength of 10.6 nm. We attempted to measure the individual layer thicknesses from the higher magnification lineplot shown in Fig. 1C but were unable to identify the individual layers. The apparent height is modulated nearly sinusoidally; this is the case for all of the current-controlled superlattices that we have imaged.

Figure 2 shows STM images of superlattices produced under potential control. The potential was modulated between 60 and 270 mV versus the saturated calomel electrode (SCE). The sample in Fig. 2A was grown with dwell times that produced a Tl-rich layer (that is, grown at 60 mV) that was 11 nm thick and a Pb-rich layer that was 34 nm thick. In the sample shown in Fig. 2B the layer widths are reversed. The Tl-rich layer in Fig. 2B was grown to be 31 nm thick, and the Pb-rich layer was grown to be 16 nm thick. The individual layers are easily identified in these potential-controlled superlattices. The layer with the lower Pb content and higher resistivity always has an apparent height in the STM image that is ~5 nm higher than the layer with the lower resistivity. Also, the images of both halves of a cleaved sample have the same profile, suggesting that the variation in apparent heights is due to differences in electrical properties rather than physical corrugation (*16*). These samples demonstrate a strength of the STM as a characterization tool as compared to x-ray diffraction. The modulation wavelengths of the two samples are too large to measure by x-ray diffraction but too small to measure by scanning electron microscopy. When the modulation wavelength of a superlattice exceeds about 20 nm, the satellites cannot be resolved from the Bragg reflection. Also, x-ray diffraction can only be used to measure the layer thicknesses if the modulation is periodic. Semiconductor quantum wells for device applications are often designed to have layer thicknesses that are outside of the x-ray diffraction regime or are nonrepeating. Because crystallinity is not required, the STM could be used to measure the layer thicknesses in nanoscale amorphous multilayers.

We prepared superlattices both galvanostatically and potentiostatically with modulation wavelengths in the 50-nm range in order to compare their apparent height profiles. We grew the superlattice in Fig. 3A by modulating the current density between 0.05 and 5 mA/cm^2, and we grew the superlattice in Fig. 3B by modulating the potential between 53 and 253 mV versus SCE. The STM image of the potential-controlled superlattice has an apparent height profile that is more square than that of the current-controlled superlattice. Also, it is possible to measure the individual layer thicknesses in the potential-controlled superlattice but not in the current-controlled superlattice.

Although the contrast mechanism for the cleaved superlattices is not presently known, it does appear that the composition profile of the superlattice manifests itself as an apparent height profile in the STM image. The height differences may result from true physical corrugation caused by surface reconstruction that is driven by strain gradients, or they may be apparent height differences that result from variations in electrical properties. The contrast does not appear to be attributable to differences in resistivity because the resistivity is low and would lead to minimal *iR* drop. The bulk resistivity trend would give an apparent height profile that is opposite to the profile that is experimentally observed. The surface resistivity may be different from that of the bulk material, and caution must be used in inferring bulk properties from surface measurements. We attribute the contrast to composition-dependent variations in either the work function or the local density of states at the Fermi level. This would be in agreement with earlier work by Osaka and co-workers on semiconductor multiple quantum wells (*16*, *17*). The large apparent height differences would be explained by nonideal response of the *z*-piezo because of a surface contamination layer on the cleaved superlattice. Scanning tunneling spectroscopy in the $d(\ln I)/ds$ and dI/dV modes should help to identify the contrast mechanism (*7*, *8*).

The STM results suggest that the composition follows the applied potential more closely than it follows the applied current. X-ray diffraction provides another measure of the squareness of the composition profile (*5*, *6*, *21*). The x-ray diffraction pattern of a superlattice that was produced by modulating the potential between 52 and 242 mV is shown in Fig. 4. The superlattice, which has an x-ray modulation wavelength of 13.4 nm and an STM modulation wavelength of 12.7 nm, has superlattice satellites out to the fourth order. The existence of higher order satellites shows that the superlattice has a relatively square composition profile. The STM has helped us engineer a ceramic superlattice with a level of perfection approaching that found in semiconductor superlattices produced by high-vacuum techniques such as molecular beam epitaxy and metal-organic chemical vapor disposition.

It should be possible to use the STM to profile the electrical properties on a nanometer scale of nearly any material that has a high enough conductivity to be imaged in the STM and that can be cleaved to produce a surface with a physical corrugation less than the apparent height variations in the image due to the local electronic properties. We have used the STM to fine-tune the synthesis and processing of nanometer-

scale ceramic superlattices. Other possible applications of the technique include mapping out the band structure and doping profile in semiconductor multiple quantum wells and studying the coherency of interfaces in superlattices by directly observing the interfacial registry of atoms in the materials.

REFERENCES AND NOTES

1. C. R. Leavens and R. Taylor, Eds., *Interfaces, Quantum Wells, and Superlattices* (North Atlantic Treaty Organization Series B: Physics, vol. 179) (Plenum, New York, 1988).
2. L. Esaki, *IEEE J. Quantum Electron.* **QE-33**, 1611 (1986).
3. C. Weisbuch and B. Vinter, *Quantum Semiconductor Structures* (Academic Press, San Diego, CA, 1991).
4. R. M. Fleming *et al.*, *J. Appl. Phys.* **51**, 357 (1980).
5. D. B. McWhan, in *Synthetic Modulated Structures*, L. L. Chang and B. C. Giessen, Eds. (Academic Press, Orlando, FL, 1985), chap. 2.
6. M. Shinn, L. Hultman, S. A. Barnett, *J. Mater. Res.* **7**, 901 (1992).
7. G. Binnig and H. Rohrer, *IBM J. Res. Dev* **30**, 355 (1986).
8. P. K. Hansma and J. Tersoff, *J. Appl. Phys* **61**, R1 (1986).
9. J. Simmons, *ibid.* **34**, 1793 (1963).
10. S. M. Sze, *Physics of Semiconductor Devices* (Wiley, New York, ed. 2, 1981), chap. 1.
11. F. Flores and N. Garcia, *Phys. Rev. B* **30**, 2289 (1984).
12. C. G. Slough *et al.*, *ibid.* **42**, 9255 (1990).
13. X. L. Wu *et al.*, *Science* **248**, 1211 (1990).
14. D. Jeon, J. Kim, M. C. Gallagher, R. F. Willis, *ibid.* **256**, 1662 (1992).
15. P. Muralt, *Surface Sci.* **181**, 324 (1987).
16. F. Osaka, I. Tanaka, T. Kato, Y. Katayama, *Jpn. J. Appl. Phys.* **27**, L1193 (1988).
17. T. Kato, F. Osaka, I. Tanaka, *ibid* **28**, 1050 (1989).
18. J. M. Gomez-Rodriguez *et al.*, *Appl. Phys. Lett.* **56**, 36 (1990).
19. J. A. Dagata *et al*, *ibid.* **59**, 3288 (1991).
20. J. A. Switzer, M. J. Shane, R. J. Phillips, *Science* **247**, 444 (1990).
21. A. Guinier, *X-ray Diffraction in Crystals, Imperfect Crystals, and Amorphous Bodies*, translated by P Lorrain and D. Sainte-Marie Lorrain (Freeman, San Francisco, 1963).
22. R. J. Phillips, M. J. Shane, J A. Switzer, *J. Mater. Res.* **4**, 923 (1989)
23. J. A Switzer, *J. Electrochem. Soc.* **133**, 722 (1986).
24. W. Mindt, *ibid.* **116**, 1076 (1969).
25. We obtained STM images with a Nanoscope II (Digital Instruments) using Pt-Ir tips. For all samples, the tunneling current was 0.5 nA and the applied bias was 200 mV with the tip positive. The scan rate was 5 Hz or less, and the scan area was approximately the same as the final image area. Fast Fourier filtering was used to remove white noise from the image. The filtering did not change the shape of the apparent height profiles Samples were imaged with several different tips to ensure that the apparent height profiles did not result from tip sharpness.
26. S. A. Chalmers *et al.* [*Appl. Phys. Lett.* **55**, 2491 (1989)] have imaged tilted superlattices in the atomic force microscope by selectively etching one of the layers to improve contrast.
27. The superlattices were deposited from a stirred solution of 5 mM $TlNO_3$ and 100 mM $Pb(NO_3)_2$ in 5 M NaOH A prelayer of $Pb_{0.74}Tl_{0.26}O_{1.9}$ with a strong (210) texture was used to control the orientation of the superlattice. The potentials and currents were controlled with a potentiostat-galvanostat (EG&G model 273A).

28. This work was supported in part by National Science Foundation grant DMR-9202872 and by Office of Naval Research grant N00014-91-J-1499.

20 July 1992; accepted 29 October 1992

Dynamics of Soil Carbon During Deglaciation of the Laurentide Ice Sheet

Jennifer W. Harden, Eric T. Sundquist, Robert F. Stallard, Robert K. Mark

Deglaciation of the Laurentide Ice Sheet in North America was accompanied by sequestration of organic carbon in newly exposed soils. The greatest rate of land exposure occurred around 12,000 to 8,000 years ago, and the greatest increase in the rate of carbon sequestration by soils occurred from 8,000 to 4,000 years ago. Sequestration of carbon in deglaciated peat lands continues today, and a steady state has not been reached. The natural rate of carbon sequestration in soils, however, is small relative to the rate of anthropogenic carbon dioxide production.

Terrestrial organic C may be an important source (*1*, *2*) or sink (*3*) for atmospheric CO_2. It is also an integral component of C cycling over glacial cycles (*4*) and may "damp" glacial cycles through release and uptake of atmospheric CO_2 (*5*). The global mass of atmospheric CO_2 (740 Gt of C, 1 Gt = 10^{15} g) is sensitive to changes in the larger pool of terrestrial C (about 2100 Gt of C), of which about two-thirds is soil organic C. Evaluation of soil C sources and sinks is difficult because the dynamics of soil C storage and release are complex and still poorly understood. When the substrate is initially free of C, net C accumulation rates are high but typically decrease manyfold as the soil develops (*1*, *6–8*). However, published inventories of soil C seldom include information about soil age and development that is necessary to estimate fluxes.

J. W. Harden and R. K. Mark, U.S. Geological Survey, Menlo Park, CA 94025.
E. T. Sundquist, U.S. Geological Survey, Quissett Campus, Woods Hole, MA 02543.
R. F. Stallard, U.S. Geological Survey, Denver Federal Center, Lakewood, CO 80225.

Rates of soil C accumulation depend on dynamic interactions among landscape, substrate, vegetation, and climate. In this report, we examine the temporal and spatial dynamics of soil C accumulation in the region formerly occupied by the Laurentide Ice Sheet. We combine soil inventories with landscape histories to model soil C sequestration (*9*) for the region during the last 18,000 years.

We quantified the area of exposure of seven generalized soil units for the past 18,000 years by combining maps of ice retreat and soils (Figs. 1 and 2) in Canada and the northern United States (*10–12*).

For most soils, rates of net C accumulation are greatest during early stages of soil development on freshly exposed substrates. Studies from diverse climatic and geologic settings (*1*, *6*) show that the rate of this accumulation in mineral soils diminishes after hundreds to thousands of years. Following the example of earlier models of soil organic C (*7*, *8*, *13*), we used a reservoir model that incorporates a zero-order input of C and a first-order rate of loss:

$$\frac{dC}{dt} = I - kC \quad (1)$$

where C is the mineral soil C mass per unit area of land surface, I is the rate of input, and k is the first-order rate constant for loss. The solution to this equation is:

$$C = I/k \times (1 - e^{-kt}) = C_e(1 - e^{-kt}) \quad (2)$$

where Ce is the equilibrium C inventory for the mineral soil. We used data from representative soil chronosequences (Fig. 3) to fit this equation (*14*). Chronosequence data were not available for Mollisols, so we used data for Brunisols instead because the C contents in these two mature soils are similar (*15*, *16*). Soils near the Rocky Mountains, Entisols and various other types, were not included because of their heterogeneity. The omission of this 0.4×10^{12} m^2 area from the total of 8×10^{12} m^2 likely resulted in an underestimate of sequestered C.

Equations 1 and 2 are not appropriate for organic soils (Histosols or peats). In these soils organic matter accumulates under water-saturated conditions that maintain plant production (input) as decomposition approaches zero. Long-term average rates of C accumulation in peats range from about 10 g m^{-2} $year^{-1}$ (*17*, *18*) to greater than 50 g m^{-2} $year^{-1}$ (*18–20*), depending on factors that are only partly understood (*18*). For comparative purposes we used two rates, 10 and 30 g m^{-2} $year^{-1}$, to model C accumulation in peat. Although constant rates for long periods are not documented anywhere (*18*), the zero-order model likely represents the dramatic differences from